ACCSCIENCE PUBLISHING

International Journal of Bioprinting

RESEARCH ARTICLE

Development of a 3D-printed polycaprolactone/magnesium phosphate composite scaffold functionalized with novel antimicrobial peptides for enhanced bone defect regeneration

Ling Zheng[1], Miao Li[1], Chen Liang[1], Wei Zu[2], and Ying Zhao[1]*

[1]Department of Stomatology, Xuanwu Hospital, Capital Medical University, Beijing, China

[2]Department of Stomatology, Xiongan Xuanwu Hospital, Xiongan, China

(This article belongs to the Special Issue: *Emerging Bioprinting Techniques for Regenerative Medicine*)

Abstract

Treating large-sized infectious bone defects is currently one of the most urgent clinical challenges that need to be addressed in clinical practice. The clinical application of autologous and allogeneic bone grafts faces numerous persistent challenges that remain unresolved. Therefore, there is an urgent need to develop a bone repair scaffold capable of large-scale production, safe for *in vivo* use, and possessing robust bone repair and anti-infective properties. In this study, a 3D-printed bone repair scaffold was fabricated using a polycaprolactone (PCL) and magnesium phosphate (MgP) composite material. The scaffold subsequently underwent surface modification with the antimicrobial peptide Tet213 with a DOPA tail, ultimately leading to the development of a novel bone repair scaffold named DTet213@PCL/MgP. The experimental results demonstrated that the DTet213@PCL/MgP scaffold exhibited outstanding antibacterial efficacy against *Escherichia coli* (*E. coli*) and *Staphylococcus aureus* (*S. aureus*), along with superior proliferation and osteogenesis capabilities for MC3T3-E1 preosteoblastic cells. In a rat radial defect model, the scaffold effectively induced new bone formation at the defect site, resulting in rapid bone regeneration. Furthermore, histopathological examination (HE staining) of major organs confirmed the excellent *in vivo* biocompatibility and safety profile of the DTet213@PCL/MgP scaffold. In the future, the DTet213@PCL/MgP scaffold represents a novel solution for the treatment of large-scale infected bone defects, capitalizing on its dual functionality in osteogenesis and infection control.

Keywords: 3D printing; Bone repair; DOPA; Magnesium phosphate; Novel antimicrobial peptide

***Corresponding author:**
Ying Zhao
(zhaoying_a@xwh.ccmu.edu.cn)

Citation: Zheng L, Li M, Liang C, Zu W, Zhao Y. Development of a 3D-printed polycaprolactone/magnesium phosphate composite scaffold functionalized with novel antimicrobial peptides for enhanced bone defect regeneration. *Int J Bioprint.* 2025;11(3):277-291. doi: 10.36922/IJB025080060

Received: February 20, 2025
Revised: March 6, 2025
Accepted: March 14, 2025
Published online: March 17, 2025

1. Introduction

Bone substitutes are required in many patients for the repair of bone defects. With the continuous development of tissue engineering technology, an increasing number of synthetic bone repair scaffolds are gradually replacing bone substitutes such as allografts.[1] Synthetic bone repair scaffolds have numerous advantages over traditional

autogenous bone substitutes, such as wide availability, no risk of transmitting infectious diseases, and the ability to be customized according to patient needs.[2,3] Although encouraging repair effects have been achieved with synthetic bone repair scaffolds, the infection problems caused by scaffold implantation have also attracted much attention. Serious infections at the implant site of the scaffold can ultimately lead to complications such as osteomyelitis.[4] Bacterial infection can lead to the formation of a biofilm on the surface of the scaffold, and the formation of this biofilm gradually induces bacterial resistance to antibiotics, posing a challenge in clinical practice.[5]

To address bacterial infections at bone defect sites, traditional treatment involves the systemic administration of antibiotics through injection. Systemic administration of antibiotics requires a large dosage, and a significant amount of antibiotics also exist in uninfected tissues and organs, which can cause toxicity to the kidneys and liver during long-term use. To reduce the side effects of systemic antibiotic administration, some studies have also directly loaded antibiotics onto the surface of scaffolds and inside filling materials to achieve local anti-infective effects. Yang et al.[6] developed a 3D-printed bone repair scaffold by directly incorporating the antibiotic ampicillin into a PCL (polycaprolactone)/Mg composite material. Experimental results have shown that this method of *in situ* release of antibiotics from a scaffold results in strong anti-infection capabilities. This method of incorporating ampicillin into the scaffold enables localized drug release at the site of bone defect infection. Compared with systemic administration, this approach requires a lower dose of antibiotics and is less prone to causing side effects.

Although antibiotics have significant therapeutic effects, their overuse has gradually led to bacterial resistance to these antibiotics.[7] The emergence of superbugs, or super-resistant bacteria, poses a significant threat to human health in the coming decades.[8] To address the increasingly urgent issue of antibiotic resistance, new technologies and drugs are needed to solve the problem of bone defect infections. In recent years, antimicrobial peptides (AMPs) have garnered widespread attention as a novel class of antimicrobial agents. The antibacterial mechanism of AMPs is highly diverse and capable of interfering with the normal growth and metabolism of bacteria at multiple levels, making them highly effective natural antimicrobial agents.[9] Therefore, AMPs are less likely to induce bacterial resistance and exhibit strong inhibitory effects against resistant bacteria.[10] In another study, Ibrahim et al.[11] blended AMPs into electrospun fibers to prepare a bone repair material with antibacterial ability. The experimental results showed that this electrospun material containing AMPs had good bactericidal ability against both gram-negative (*Escherichia coli*) and gram-positive (*Staphylococcus aureus*) bacteria. The results of cell compatibility experiments also indicated that AMPs had good cell compatibility and no significant cytotoxicity. As novel antibacterial agents, AMPs have significant advantages in countering infections associated with bone defect.

Bone repair scaffolds should possess a potent capacity for promoting bone formation. To improve the osteogenic effect of scaffolds, some bioactive materials are often added to them. Owing to its ability of slowly Mg^{2+} and PO_4^{3-} release, $Mg_3(PO_4)_2$ (MgP) has been used as a bioactive molecule in bone repair materials to promote the repair of bone defects. Lei et al.[12] incorporated varying proportions of MgP into PCL to develop a bone repair scaffold. The scaffold containing 20% MgP demonstrated excellent efficacy in repairing rabbit maxillofacial bone defects. As a bioactive molecule for bone repair, MgP has several advantages over Mg metal in the field of bone repair. Mg is prone to release hydrogen gas *in vivo*, creating an alkaline environment that can trigger inflammatory reactions. The release of PO_4^{3-} from MgP can accelerate bone induction and mineralization.

To address the challenge of achieving efficient binding between AMPs and scaffolds, this study drew inspiration from the mussel protein adhesion mechanism and innovatively modified AMPs by introducing a YKYKY tag at their termini. The tyrosine residues in the YKYKY sequence can be enzymatically converted to adhesive DOPA molecules under the catalysis of hydroxylase. We hypothesize that these DOPA-AMPs exhibit enhanced binding affinity to scaffold materials and possess sustained-release capabilities. To simultaneously endow the scaffold with osteoinductive properties, we incorporated 20% MgP into PCL and fabricated the scaffold via 3D printing using the MgP/PCL composite. We anticipate that MgP will release Mg^{2+} during scaffold degradation, which may promote bone repair through the Wnt signaling pathway. The characteristics of this dual-functional bone repair scaffold were systematically evaluated through *in vitro* and *in vivo* experiments to explore its potential therapeutic efficacy for infected tibial defects in rat models.

2. Materials and methods

2.1. 3D-printed MgP/PCL scaffolds modified with surface AMPs

PCL (M_W = 80,000) and MgP were purchased from Shanghai Aladdin Biochemical Technology Co., Ltd. (China). Eighty gram of PCL and 20 g of MgP were weighed separately, mixed together, and then placed into a small internal mixer (MIX002, Ubbiotech, China). The materials were mixed at

80°C for 20 min. After mixing was complete, the composite material was cut into particles with a diameter of less than 8 mm. The dimensions of the scaffold were designed via SolidWorks 2020, and the printing parameters were set via simplified 3D software. The 5 g composite particles were placed into the printing tube, and then the scaffold was printed via a 3D printer (3Dcreactor03, Ubbiotech, China). The printing temperature was set at 80°C, with a nozzle diameter of 0.3 mm, a printing speed of 8 mm/s, a printing bed temperature of 4°C, and a 45% fill rate. FITC-labeled Tet213 (KRWWKWWRRC), Y-Tet213 (KRWWKWWRRCYKYKY), and FITC-labeled Y-Tet213 were synthesized by BGI Genomics Co., Ltd. (China). According to methods reported in previous studies, the tyrosines in both FITC-Y-Tet213 and Y-Tet213 were hydroxylated to DOPA molecules.[13] Using the above methods, we successfully prepared the AMP DOPA-Tet213 (DTet213). The scaffold was then soaked in DTet213 solution and incubated in a 4°C shaker at 60 rpm for 12 h. After the scaffolds were incubated in AMP solution, they were washed three times with phosphate-buffered saline (PBS) for 5 min each to remove unbound AMP. A scaffold with a DTet213-modified surface can be obtained via the above method.

2.2. Optimization of the DTet213 AMP concentration

To investigate the effect of the DTet213 concentration on antibacterial activity, we coated the surface of PCL#MgP scaffolds (10 mm × 10 mm × 2 mm) with various concentrations of DTet213 (1, 0.5, and 0.25 mg/mL). *E. coli* and *S. aureus* were used to evaluate the antibacterial effects of different concentrations of DTet213. The scaffolds were immersed in bacterial suspensions of *E. coli* and *S. aureus* containing 4.0×10^4 bacteria/mL. The samples were then incubated in a constant-temperature shaker at 37°C with shaking at 150 rpm for 12 h. After that, 100 μL of the bacterial suspension was spread onto LB agar plates and further incubated for 24 h. The bacterial clones on the agar plates were photographed using a camera, and the colonies were counted via ImageJ 1.53e software (NIH, USA).

2.3. Physical and chemical characterization of the scaffold

The surface morphology of the scaffolds was observed by scanning electron microscopy (SEM; Gemini2 ZEISS, Germany). The appearance and porosity of the scaffolds were scanned and analyzed via micro-CT (SkyScan 1172 Bruker, Belgium). The tensile strength and compressive strength of the scaffolds were tested via a universal mechanical testing machine (6800 Instron, UK). The hydrophilicity of the scaffold surface was measured via a water contact angle (WCA) meter (DSA25S KRUSS, Germany). The chemical components of the scaffolds were characterized by Fourier transform infrared spectroscopy (FTIR, TENSOR 27, Bruker).

2.4. Scaffold degradation capability and Mg^{2+} release characteristics

PCL#MgP scaffolds (10 mm × 10 mm × 2 mm) were immersed in PBS solutions containing 0.4 mg/mL lipase and 1 mg/mL sodium azide for degradation experiments. Then, the centrifuge tubes containing the scaffolds were placed in a shaker (100 rpm, 37°C) for incubation. At the 5th, 10th, and 15th days, the scaffolds were removed from the degradation solution, dried, and then weighed after drying. The degradation rate (%) of the scaffolds was calculated using **Formula I**.

$$\text{Degradation rate (\%)} = (W_0 - W_t)/W_0 \times 100\% \quad \text{(I)}$$

where W_0 is the starting weight and W_t is the timepoint weight.

The scaffolds (10 mm × 10 mm × 2 mm) of different groups were separately immersed in 40 mL of deionized water, and then, the centrifuge tubes containing them were placed in a shaker for incubation (10 rpm, 37°C). Every 4 days, a 50 μL sample of the release solution was collected. The scaffolds continued to release Mg^{2+} for a total of 20 days. Inductively coupled plasma-mass spectrometry (ICPMS; Varian, Darmstadt, Germany) was subsequently used to detect Mg in the release solution.

2.5. The binding capacity and release characteristics of AMPs with scaffolds

The scaffolds (10 mm × 10 mm × 2 mm) were separately immersed in solutions of FITC-labeled DTet213 (0.5 mg/mL), FITC-labeled Tet213 (0.5 mg/mL), and PBS at 4°C with a shaking speed of 60 rpm for 12 h. The PBS group was used as the negative control group. Subsequently, the scaffolds were gently washed three times for 5 min in PBS. Finally, the scaffolds were photographed via a fluorescence imaging system (IVIS Spectrum PE, USA). The mean fluorescence intensity of the scaffolds was quantitatively calculated via software. The scaffolds coated with FITC-labeled DTet213 and FITC-labeled Tet213 were placed into 24-well plates. Subsequently, 1 mL of PBS was added to each well, and the plates were incubated in a constant temperature shaker at 37°C and 50 rpm. At time intervals of 1, 3, 6, 12, 24, 48, and 72 h, 100 μL of the solution was aspirated for relative fluorescence intensity (RFI) measurement using a multifunctional microplate reader (M200, Tecan, Switzerland). After measurement, the sampled solution was returned to the release system.

2.6. Cytocompatibility and osteogenesis

MC-3T3-E1 cells were used to evaluate the cell adhesion capacity and cell proliferation capacity of the scaffolds. The cells were cultured in Dulbecco's modified Eagle's medium (DMEM) at 37°C, 0.5% CO_2, and 100% humidity. The medium was changed every 2 days. When the cell density exceeded 90%, the cells were digested with trypsin and then subcultured into new cell culture dishes. The scaffold was sterilized by exposure to ultraviolet (UV) light for 2 h. The scaffold was placed into a 50 mL centrifuge tube with a ventilated cap, and the cells were seeded onto the surface of the scaffold at a density of 1×10^5 cells/mL. To increase the opportunity for cell–scaffold contact, the centrifuge tube containing the cells and scaffold was placed on a shaker that can perform programmed shaking. After 12 h of oscillatory culture, the scaffold was transferred to a 6-well plate and further cultured for 3 days. After the culture was complete, the cells were washed three times with PBS, and then live/dead staining solution was added to the cells for staining at 37°C for 30 min. After staining was complete, the cells were washed three times with PBS and then photographed via a fluorescence-inverted microscope. CCK-8 working solution was added to the scaffolds, which were further incubated in the incubator for 30 min. The OD450 absorbance value was subsequently read via a plate reader (M200 Tecan, Switzerland). Cells cultured on different materials for 3 days were subjected to Runx2 immunofluorescence staining analysis. Firstly, the cells were fixed with glutaraldehyde for 5 min, washed three times with PBS, and then incubated with Alexa Fluor 488-conjugated phalloidin for 30 min to stain the cytoskeleton. Subsequently, the cells were incubated with rabbit anti-mouse Runx2 primary antibody (Proteintech, China) for 2 h, followed by incubation with Alexa Fluor 555-conjugated goat anti-rabbit secondary antibody (Proteintech, China) for 2 h. Finally, the cells were imaged using a fluorescence microscope (TE2000-U, Nikon, Japan).

2.7. Repair of tibial defects in rats

Twelve male Sprague–Dawley rats (each weighing approximately 150 g) were selected for *in vivo* experiments on the repair of radial bone defects. The animals were anesthetized via a respiratory anesthesia machine with isoflurane. The hind leg of each animal was shaved, and then a surgical blade was used to cut through the skin to expose the tibia. Next, an electric drill was used to create a 2.5 mm diameter circular defect on the tibial plateau. Ten microliters of a mixed bacterial suspension containing *E. coli* and *S. aureus* (4.0×10^4 bacteria/mL) were applied to the bone defect site. Different groups of scaffolds were implanted into the defect sites, and then the wounds were surgically sutured. At 8 weeks post-surgery, the animals were euthanized, and then the tibiae were scanned via micro-CT (Skyscan 1172 Bruker, Belgium). 3D reconstructed images of the bone at the defect site were created via the CTVox software (Bruker, Belgium). The bone volume/tissue volume (BV/TV), trabecular thickness (Tb.Th), trabecular number (Tb.N), and trabecular separation (Tb.SP) of the new bone were calculated via the CTan software (Bruker, Belgium).

2.8. Histological evaluation

The bone samples were immersed in a 4% paraformaldehyde solution for fixation. The bone samples were subsequently immersed in a 10% ethylenediaminetetraacetic acid (EDTA) solution for decalcification. The bone defect tissue was trimmed and then embedded in paraffin. The bone samples were cut into 5 μm slices and subsequently subjected to hematoxylin and eosin (H&E), Masson, Sirius red, and osteopontin (OPN) histochemical staining to evaluate tissue regeneration.

2.9. Statistical analysis

The data are presented as the means ± standard deviations. The significance of differences between the groups for the different printability and mechanical parameters was assessed via one-way analysis of variance (ANOVA) and post hoc Tukey's test (OriginPro 2024). Differences were considered significant at a probability error (p) of $p < 0.05$.

3. Results and discussion

3.1. Antibacterial ability of the scaffold

As shown in Figure 1, the PCL#MgP scaffold had no obvious antibacterial effect on *E. coli* or *S. aureus*, and the number of bacterial clones on the agar plate was greater than 900. There were significantly fewer clones of *E. coli* and *S. aureus* on Agar plates in the 0.25@PCL#MgP group than in the PCL#MgP group. The number of *E. coli* and *S. aureus* clones decreased by 66.88% and 66.45%, respectively. The bacterial clone numbers of *E. coli* and *S. aureus* in the 0.5@PCL#MgP group and the 1@PCL#MgP group were reduced to below 50, and there was no significant difference between the two groups. These results indicate that the antibacterial activity of the scaffold is closely related to the AMP concentration. When more AMPs were attached to the scaffold surface, the antibacterial ability of the scaffold was also enhanced. When a certain concentration is reached, the antibacterial ability also reaches the maximum level. In this study, when the concentration of DTet213 used for surface-modified scaffolds reached 0.5 mg/mL, the scaffolds showed excellent resistance to *E. coli* and *S. aureus*. There was no significant difference in antibacterial activity between 1 mg/mL DTet213 and 0.5 mg/mL DTet213. Due to the unique antimicrobial mechanism of

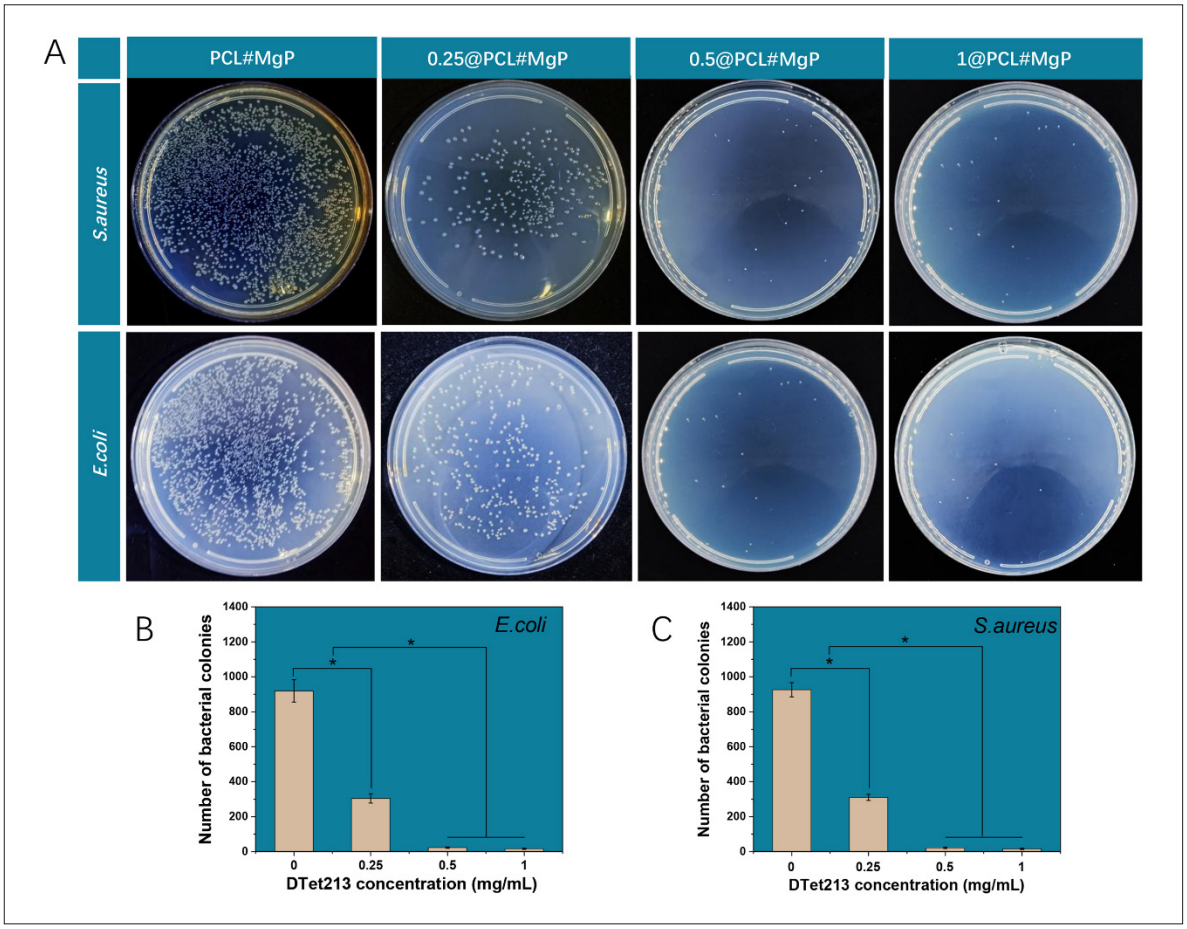

Figure 1. Antibacterial ability of scaffolds with different concentrations of Tet213. (A) Bacterial colony images. (B) Number of *E. coli* colonies. (C) Number of *S. aureus* colonies. $n = 3$; $^*p < 0.05$.

AMPs, it is difficult for bacteria to develop resistance to AMPs.[14] However, while AMPs kill bacteria, they can also cause cytotoxicity to mammalian cells.[15] Therefore, while ensuring good antibacterial ability, the use of AMPs should be minimized. On the basis of the above characteristics of AMPs, 0.5 mg/mL DTet213 (0.5@PCL#MgP) was selected for subsequent experiments in this study.

The amphipathic structure of AMPs enables them to selectively bind to bacterial cell membranes, forming transmembrane pores that disrupt membrane integrity and exert bactericidal effects. Additionally, AMPs can directly penetrate bacterial cells to act on specific intracellular targets, interfering with normal bacterial growth and metabolic balance, thereby achieving bactericidal outcomes. They exhibit universal antibacterial activity and are less prone to developing drug resistance.[16,17] Given the numerous advantages, AMPs are more expensive than traditional antibiotics. AMPs can only exert their full antibacterial effects when reaching effective concentrations, and whether high-dose administration *in vivo* may cause side effects requires further investigation.[18] To achieve both low-dose usage *in vivo* and ensured bactericidal efficacy, this study introduced a DOPA tag at the C-terminal of AMPs. This tag enables firm adhesion of AMPs to scaffold surfaces, which helps avoid initial burst release to some extent and facilitates sustained slow release over extended periods, thereby enhancing the antimicrobial effects *in vivo*.

3.2. Scaffold structure

As shown in Figure 2A, the scaffolds of all the groups appeared white in appearance. After the addition of MgP to PCL, there was no significant change in the color of the scaffolds. Similarly, there was no notable change in color after the scaffolds were surface-modified with DTet213. To better observe and analyze the internal pore structure of the scaffold, we performed micro-CT scanning and 3D reconstruction of the scaffold. As shown in Figure 2B, the pore structure of the surface of the scaffold was arranged regularly and orderly, and the pore structure between the

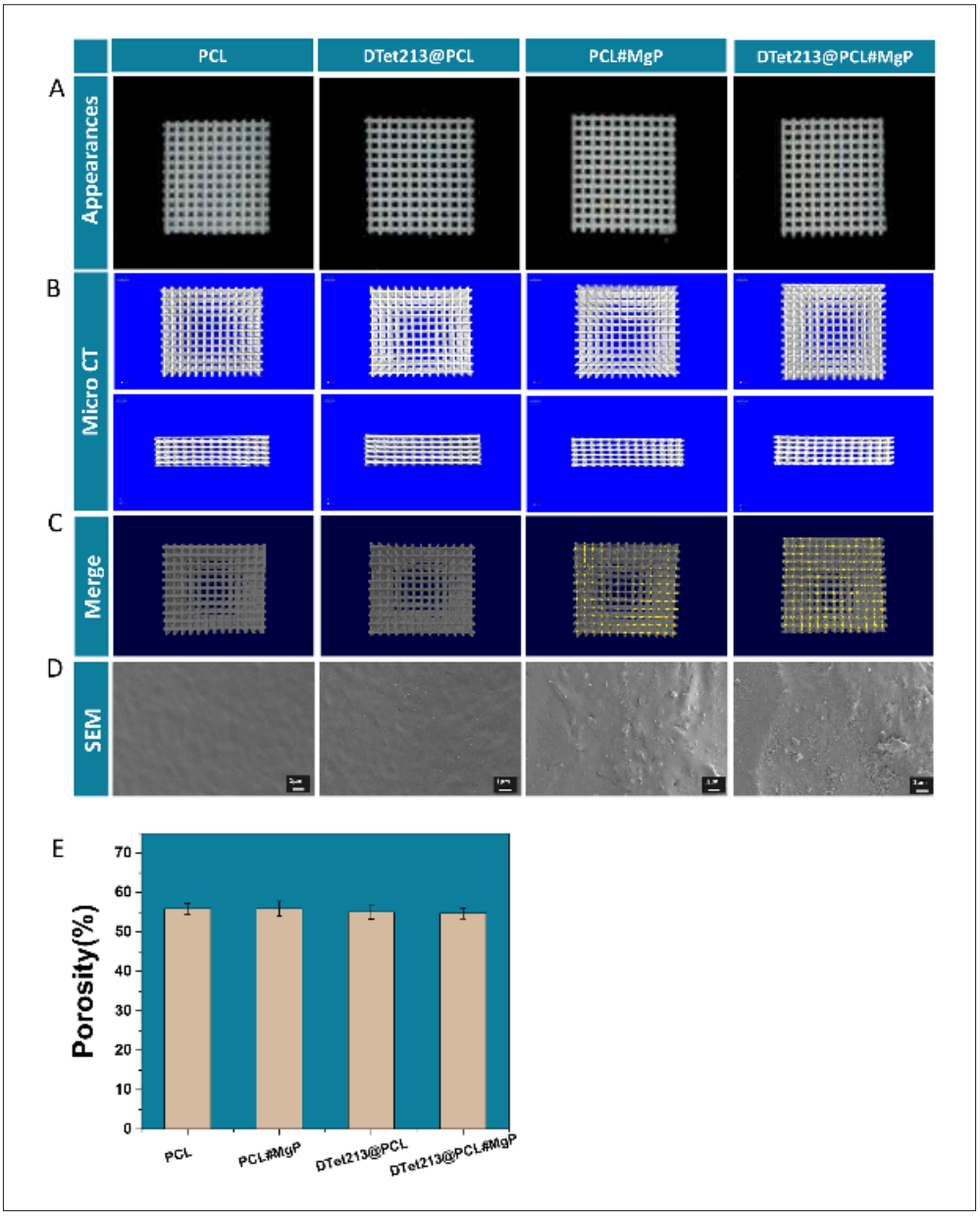

Figure 2. Macroscopic and microscopic morphology of different groups of scaffolds. (A) Appearance, (B) micro-CT reconstruction, (C) PCL/MgP merged, and (D) SEM images of different groups of 3D-printed scaffolds; scale bar: 1 μm. (E) Scaffold porosity, $n = 3$.

layers of the scaffolds was clearly visible. CTAn software (Bruker, Belgium) was used to split the PCL and MgP components in the scaffold by adjusting the gain value, and CTvol software (Bruker, Belgium) was used to merge and reconstruct the PCL and MgP components. As shown in Figure 2C, the material of the scaffolds in the PCL and DTet213@PCL groups was PCL (gray), and no MgP (yellow) component was found. The scaffolds in the PCL#MgP and DTet213@PCL#MgP groups had a significant presence of MgP components on their surfaces. As shown in Figure 2D, the SEM images revealed that the surface of the scaffolds in the PCL group was smooth, a small number of particles were deposited on the surface of the scaffolds in the DTet213@PCL group, and the scaffolds in the PCL#MgP and DTet213@PCL#MgP groups were rough, with many particles deposited on the surface of the scaffolds. As shown in Figure 2E, CTAn software was used to analyze the porosities of the different groups of scaffolds,

and the porosities of all the groups of scaffolds were not significantly different, ranging from 54.76% to 55.94%.

3.3. Mechanical properties

As shown in Figure 3A, we prepared 3D-printed scaffolds for compression and tensile testing. The scaffold for compressive strength and tensile strength testing consisted of a 10 mm × 10 mm × 10 mm cube and a 10 mm × 40 mm × 40 mm cuboid. As shown in Figure 3B, the compressive strengths of the PCL, DTet213@PCL, PCL#MgP, and DTet213@PCL#MgP samples were 4.13 ± 0.26, 4.15 ± 0.15, 4.65 ± 0.17, and 4.69±0.21 MPa, respectively. Compared with the addition of PCL alone, the addition of MgP significantly increased the compressive strengths of the PCL#MgP and DTet213@PCL#MgP groups by 12.59% and 13.56%, respectively. The PCL surface modified with DTet213 had no significant effect on the compressive strength of the scaffold. As shown in Figure 3C, the tensile strengths of the PCL, DTet213@PCL, PCL#MgP, and DTet213@PCL#MgP scaffolds were 3.78 ± 0.45, 3.83 ± 0.36, 3.18 ± 0.16, and 3.18 ± 0.214 MPa, respectively. When 20% MgP was added to the PCL material, the tensile strength of the scaffold was significantly lower than that of the PCL material. Compared with those of the PCL group, the tensile strengths of the PCL#MgP and DTet213@PCL#MgP groups were 18.34% and 17.98% lower, respectively. The mechanical properties of scaffolds are also important factors in evaluating whether scaffolds are suitable for bone defect repair. These results show that the addition of MgP can affect the mechanical properties of PCL scaffolds. The addition of MgP to PCL resulted in an increase in compressive strength and a decrease in tensile strength. Lei et al.[12] prepared PCL scaffolds containing different proportions of MgP, and the mechanical test results of the raw materials and scaffolds were basically consistent with the results of this study. The addition of MgP can improve the poor compressive strength of PCL materials.

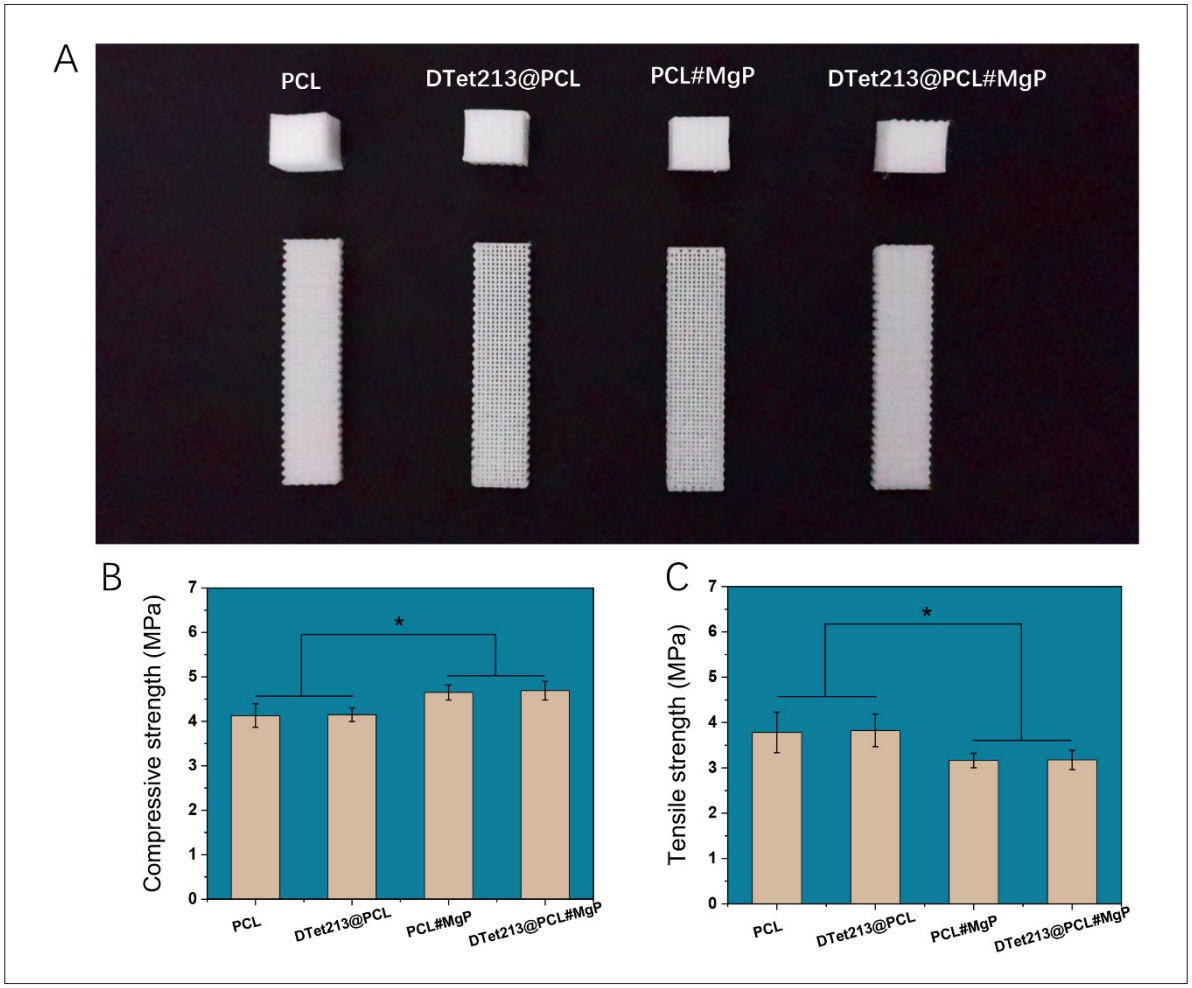

Figure 3. Mechanical properties of each group of scaffolds. (A) Appearance of test scaffolds, (B) compressive strength, and (C) tensile strength, $n = 3$, $^*p < 0.05$.

3.4. Scaffold hydrophilicity, degradability, Mg^{2+} release, and DTet213 binding ability

As shown in Figure 4A, the hydrophilicity of the different groups of scaffolds was measured in terms of WCA. The WCAs of the PCL, PCL#MgP, DTet213@PCL, and DTet213@PCL#MgP groups were 113.1 ± 5.4°, 99.03 ± 2.6°, 53.07 ± 5.0°, and 43.43 ± 4.6°, respectively. After the addition of 20% MgP to PCL, the surface hydrophilicity of the scaffold increased. When DTet213 was attached to the scaffold surface, the hydrophilicity of the scaffold was significantly increased, from a hydrophobic surface to a hydrophilic surface. The WCA of a scaffold can affect its cell adhesion capacity. Ardhaoui et al.[19] reported that a 65° WCA surface was the most favorable for osteoblast adhesion, whereas WCA values that were too high or too low were unfavorable for osteoblast adhesion. As shown in Figure 4B, FTIR analysis was used to analyze the presence of MgP and AMP in the scaffold. The peaks at 1012, 1047, 1089, and 1134 cm^{-1} in the PCL#MgP group were attributed to the asymmetric stretching vibration peaks of PO_3. The 1618 cm^{-1} peak in the DTet213@PCL group was attributed to the stretching vibration peak of the amide bond in the polypeptide.

As shown in Figure 4C, the degradation behavior of different groups of scaffolds with respect to lipase was evaluated. On the 15th day of degradation, the degradation rates of PCL, PCL#MgP, DTet213@PCL and DTet213@PCL#MgP were 6.03%, 17.63%, 23.45%, and 25.53%, respectively. The addition of 20% MgP to PCL increased the degradation rate of the scaffold. When DTet213 was attached to the surface of the scaffold, the degradation rate of the scaffold significantly accelerated. The degradation rates of DTet213@PCL and DTet213@PCL#MgP were 3.89 times and 4.23 times greater than those of the PCL group, respectively. These findings indicate that the degradation rate of the scaffold may be correlated with its surface hydrophilicity, as surfaces with greater hydrophilicity are more prone to contact lipase solutions, thereby enhancing the lipase-catalyzed cleavage of ester bonds in PCL molecules.[20]

As shown in Figure 4D, the Mg^{2+} release behavior of the different groups of scaffolds was detected. The PCL#MgP and DTet213@PCL#MgP scaffolds slowly released Mg^{2+} during the entire 20-day release period. The PCL and DTet213@PCL scaffolds do not contain Mg, so there is no release of Mg^{2+}. On the 20th day, the Mg^{2+} concentration released from the PCL#MgP and DTet213@PCL#MgP scaffolds reached 50.10 and 54.07 mM, respectively. Since MgP is slightly soluble in water, the MgP in the scaffold is gradually exposed to the release solution with the degradation of PCL, resulting in the slow release of Mg^{2+} in the scaffold. The sustained release of Mg^{2+} ensures continuous promotion of the osteogenic differentiation of cells throughout the bone regeneration period.

As shown in Figure 4E, DTet213 demonstrated a high binding ability to the scaffold compared to Tet213 without the DOPA tag. The control group scaffold surface showed almost no green fluorescence, whereas the Tet213 group scaffold surface exhibited weak green fluorescence. In contrast, the DTet213 scaffold surface displayed a significant amount of fluorescence. The mean fluorescence intensity of the DTet213 group was 1.69 times greater than that of the Tet213 group. The addition of a DOPA tail to Tet213 can significantly enhance its ability to bind to the scaffold surface, thereby improving the antibacterial properties of the scaffold. As shown in Figure 4F, Tet213 exhibited a burst release characteristic within the 6-h release period, and its cumulative release essentially reached a plateau after 12 h. In contrast, DTet213 demonstrated a sustained-release profile over the course of 72 h. The above results indicate that modifying the AMPs with a DOPA tag at its terminus not only significantly enhances the binding capacity of the AMPs with scaffold but also facilitates a sustained-release effect from scaffold. This modification endows the scaffold with a more potent and enduring anti-infective capability. Zhang et al.[21] incorporated AMPs into GelMA hydrogels, which were then used to fill the pores of 3D-printed scaffolds to facilitate the release of AMPs. While this method enables the release of AMPs at the site of infectious bone defects, the complete filling of the scaffold pores with hydrogel could potentially hinder the adhesion, proliferation, and differentiation of cells within these pores. The adhesion, proliferation, and differentiation of bone marrow mesenchymal stem cells (BMSCs) on the scaffold surface are important for bone defect repair. The AMPs designed in this study do not compromise the pore structure of the scaffold. AMPs with DOPA tag can adhere to the scaffold surface, thereby addressing the problem of the GelMA AMPs delivery method.

3.5. Cell adhesion and proliferation ability

As shown in Figure 5A, the results for cell adhesion ability on the surfaces of the scaffolds from the different groups indicate that the number of cells adhering to the surface of the PCL scaffolds was the lowest. In contrast, the number of cells adhering to the surface of the scaffolds in the DTet213@PCL group increased significantly. Compared with that in the DTet213@PCL group, the number of cells adhering to the scaffolds in the PCL#MgP group further increased. The DTet213@PCL#MgP group presented the greatest number of adhered cells. Almost all the cells on the scaffolds in all the groups were alive, with only a very small number of dead cells. As shown in Figure 5C, cell proliferation on the scaffolds of the PCL#MgP and DTet213@PCL#MgP groups

was significantly greater than that on the PCL group. The results of cell adhesion and proliferation indicate that the addition of 20% MgP to PCL and surface modification with DTet213@PCL both significantly enhance the cell adhesion and proliferation capabilities of the scaffolds. Promoting cell adhesion and proliferation on scaffolds is a basic requirement for obtaining scaffolds with potential bone repair capabilities. Although PCL is a biodegradable material approved by the Food and Drug Administration (FDA) for use and possesses high biocompatibility and safety for *in vivo* applications, it is still a bioinert material that is unfavorable for cell adhesion and proliferation. The addition of MgP effectively enhanced the bioactivity of the MgP/PCL composite materials. The WCA of a scaffold is also an important factor affecting cell adhesion. As shown in Figure 4A, when MgP was added to PCL, the hydrophilicity of the scaffold significantly improved. Furthermore, when the surface of the scaffold was modified with DTet213, the hydrophilicity of the scaffold increased further. Ardhaoui et al.[19] reported that osteoblasts demonstrate the strongest adhesion capacity on surfaces with a contact angle of 65°. Both excessively hydrophilic and excessively hydrophobic surfaces can decrease the adhesion of cells.

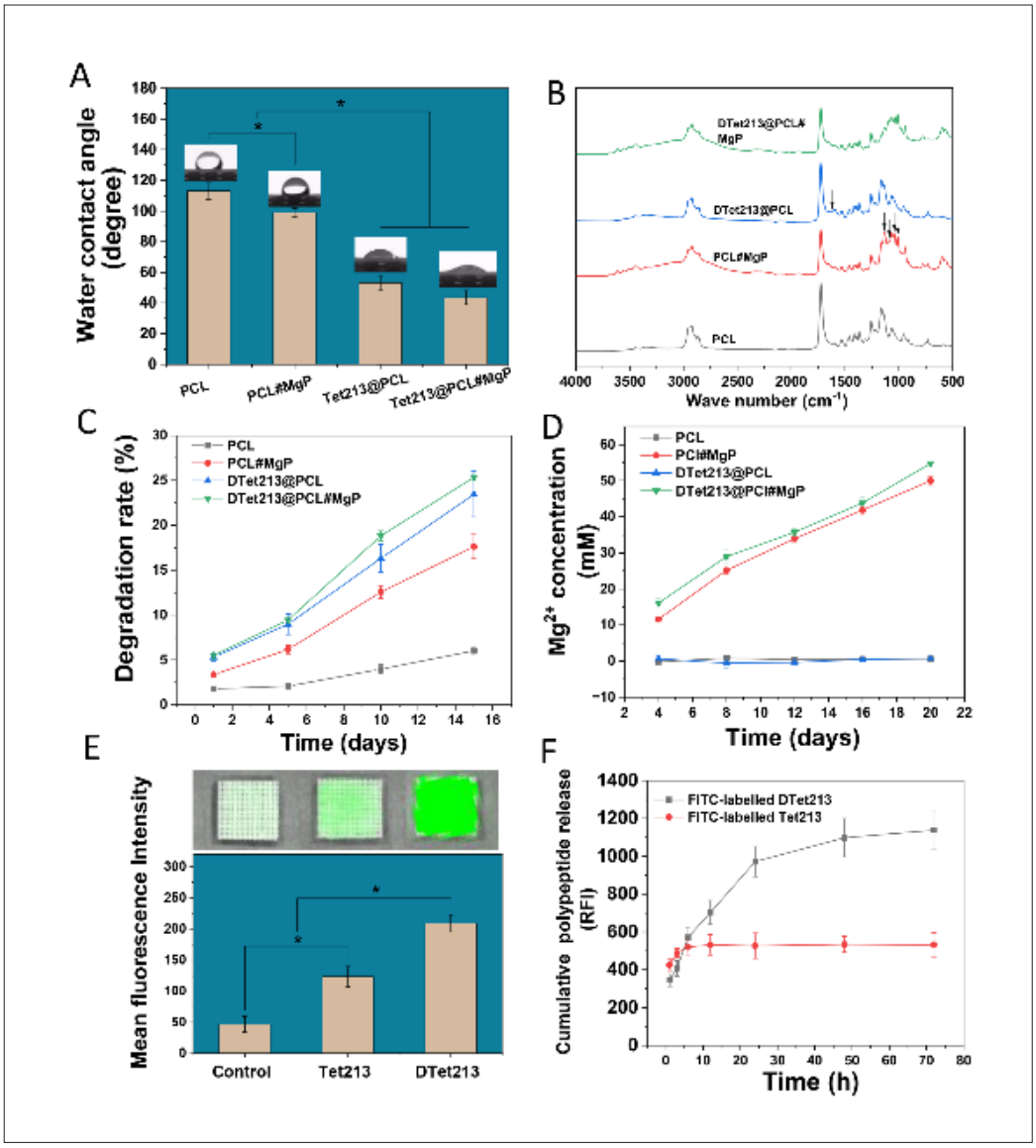

Figure 4. Scaffold characterization. (A) WCA detection; (B) FTIR analysis; (C) scaffold degradation rate; (D) scaffold Mg^{2+} release properties; (E) AMP binding ability; and (F) cumulative release profile of different groups of scaffolds. $n = 3$; $^*p < 0.05$. Abbreviations: AMP, antimicrobial peptide; FTIR, Fourier transform infrared spectroscopy; WCA, water contact angle.

As shown in Figure 5B, the experimental results showed that the Runx2 protein expression by cells in the PCL group and the DTet213@PCL group was low. In contrast, cells growing on the surface of the MgP-containing material showed a high level of Runx2 protein expression. As shown in Figure 5D, the mean fluorescence intensities in the PCL#MgP and DTet213@PCL#MgP groups were 2.23 and 2.16 times that of the PCL group, respectively. Runx2 is a key early regulator in the differentiation process of mesenchymal stem cells into osteoblasts. It can activate a series of gene expression programs related to osteoblast differentiation, prompting mesenchymal stem cells to differentiate directionally into osteoblastic lineage cells.[22] The experimental results demonstrated that both PCL#MgP and DTet213@PCL#MgP materials significantly promoted the expression of the *Runx2* gene, which was primarily attributed to the sustained release of Mg^{2+} from these materials. Studies have demonstrated that Mg^{2+} can promote osteogenic differentiation of cells through multiple mechanisms, including activation of the Wnt/β-catenin signaling pathway, upregulation of osteogenesis-related gene expression (such as *Runx2* and *OCN*), and modulation of the RANKL/OPG system balance.[23–25] Therefore, MgP incorporated into the materials in this study is expected to play a crucial biological role in bone defect repair.

3.6. Repair of bone defects

Different groups of scaffolds were implanted into tibial defects in rats. After 8 weeks of repair, the repair effect on the defects was evaluated via micro-CT. As shown in Figure 6A, the macroscopic view and defect view images revealed that the defects in the PCL and DTet213@PCL groups did not close well, and the 3D reconstructed images revealed that large defects were still present. The bone

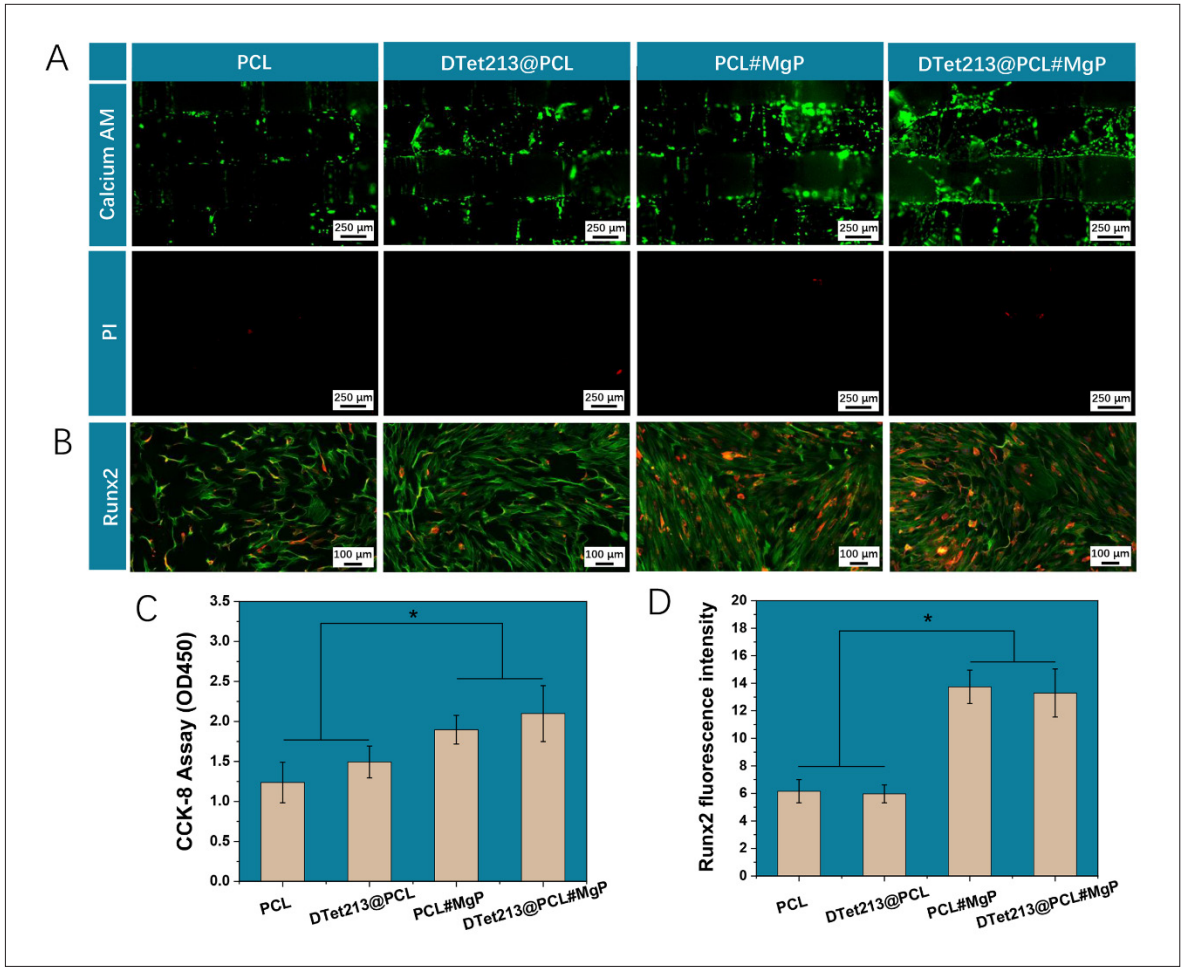

Figure 5. Cell adhesion and proliferation ability of different groups of scaffolds. (A) Calcein AM and PI staining of live (green) and dead cells (red), respectively. (B) Immunofluorescence staining (green: phalloidin staining, red: Runx2 staining). Scale bars: 250 μm (A); 100 μm (B). (C) CCK-8 assay. (D) The mean fluorescence intensity of Runx2. $n = 3$; $^*p < 0.05$.

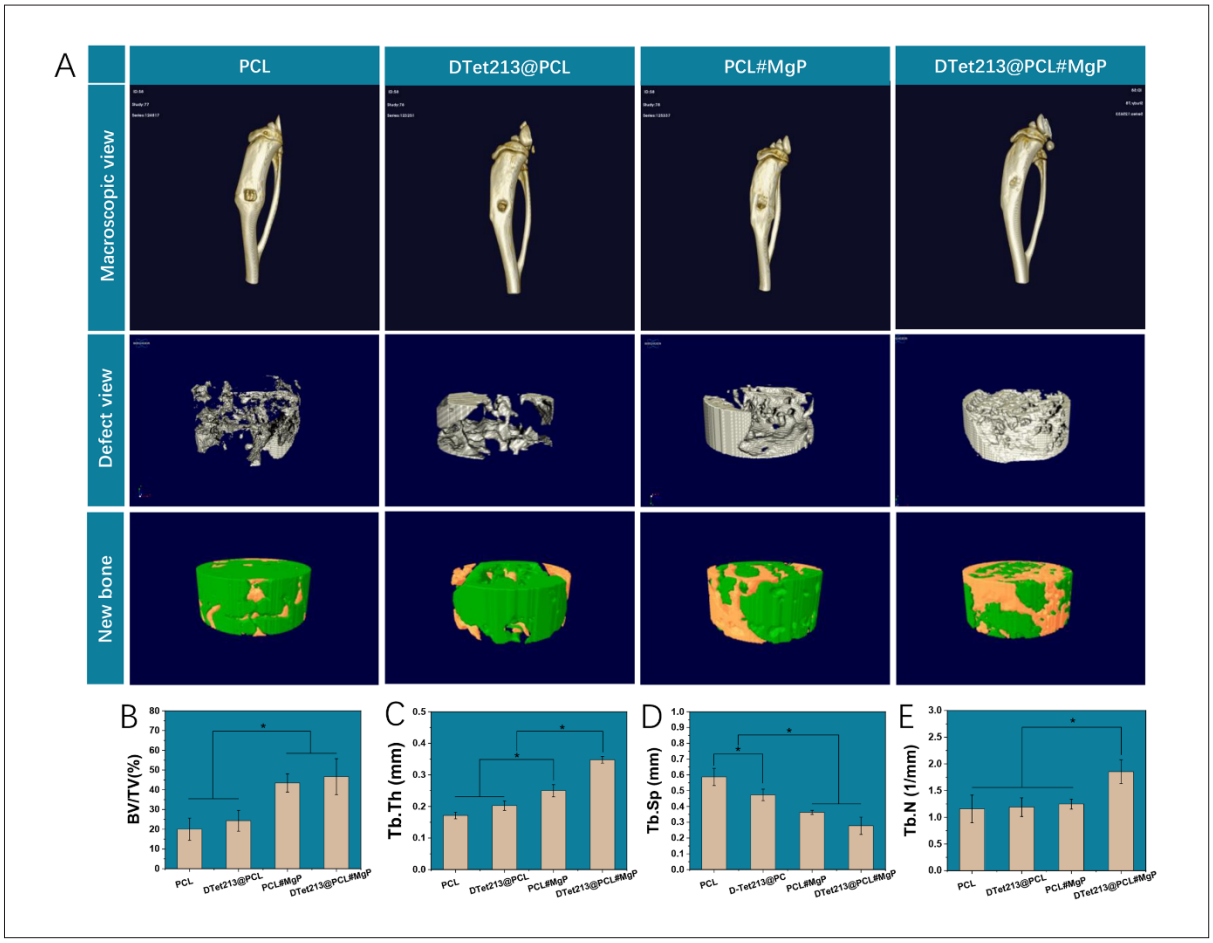

Figure 6. Evaluation of the repair effect on bone defects 8 weeks postsurgery via micro-CT. (A) 3D reconstruction images, (B) BV/TV, (C) Tb.Th, (D) Tb.Sp, and (E) Tb.N, $n = 3$; $^*p < 0.05$. Abbreviations: BV/TV, bone volume/tissue volume; Tb.N, trabecular number; Tb.Sp, trabecular separation; Tb.Th, trabecular thickness.

defect size in the PCL#MgP group decreased, with only a small part of the defects still not fully healed. The DTet213@PCL#MgP groups exhibited nearly complete closure of the bone defects. The merged images of the scaffolds and new bone at the defect site revealed that the PCL and DTet213@PCL groups were predominantly composed of scaffolds, with relatively little new bone formation. In the PCL#MgP group, more new bone formed, whereas new bone comprised the majority in the DTet213@PCL#MgP group. As shown in Figure 6B, the BV/TV values for the PCL, DTet213@PCL, PCL#MgP, and DTet213@PCL#MgP groups were 20.03 ± 5.62%, 24.29 ± 5.29%, 43.47 ± 4.63%, and 46.63 ± 9.12%, respectively. The BV/TV values of the PCL#MgP group and the DTet213@PCL#MgP group were 2.17 times and 2.33 times greater than those of the PCL group, respectively. As shown in Figure 6C, the Tb.Th of the DTet213@PCL#MgP group reached 0.3478 mm, which was significantly higher than that of the other groups. As shown in Figure 6D, the Tb.Sp of the PCL#MgP and DTet213@PCL#MgP groups were 0.3628 and 0.2776 mm, respectively, which were significantly lower than those of the PCL and DTet213@PCL groups. As shown in Figure 6E, the Tb.N of the DTet213@PCL#MgP group reached 1.85421/mm, which was significantly higher than that of the other groups.

The primary processes of bone repair encompass five phases as follows: inflammation, vascularization, cell recruitment, osteogenic differentiation, and fracture healing.[26] Severe bacterial infection at the bone defect site, if not effectively controlled, can prolong the inflammatory phase and disrupt the entire physiological process of bone repair. In previous studies, 3D-printed scaffolds made from PCL#MgP composites have been utilized for bone repair.[12,27] Our study results found that PCL#MgP scaffolds are less effective in repairing infectious bone defects

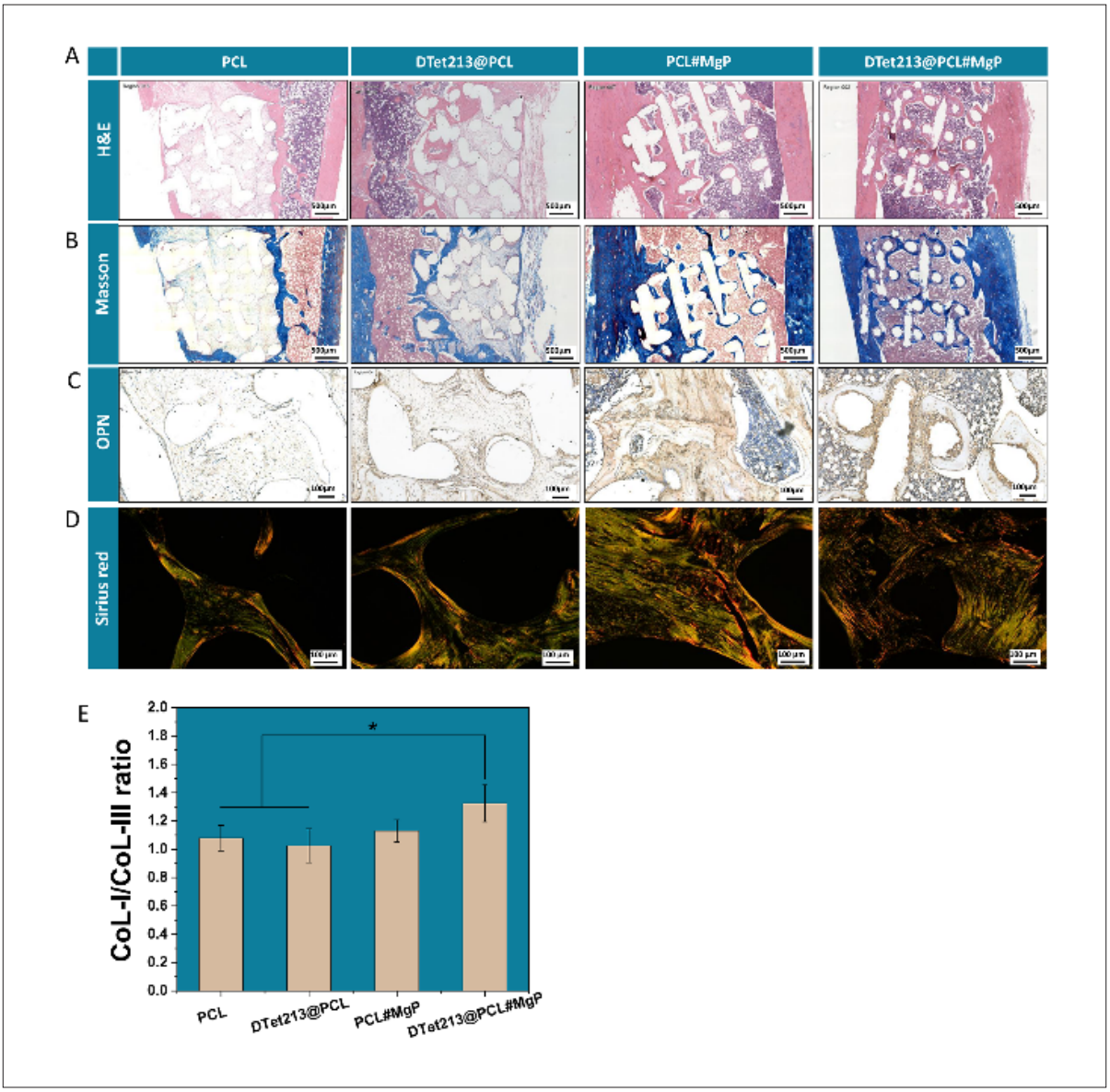

Figure 7. Histological staining analysis of the repair capacity of different scaffold groups in bone defects. (A) HE staining, Masson staining, OPN immunohistochemical staining, and Sirius red staining after 8 weeks of bone defect repair. Scale bars: 500 μm (the first 3 rows); 100 μm (the last row). (B) The COL-I/COL-III ratio in the Sirius red staining images. $n = 3$; $^*p < 0.05$. Abbreviations: COL, collagen; HE, hematoxylin and eosin; OPN, osteopontin.

compared to DTet213@PCL#MgP. Since many patients with bone defects often suffer from infections, DTet213@PCL#MgP can effectively control infections and shorten the inflammatory phase of bone repair, making it more clinically valuable than PCL#MgP scaffolds.

3.7. Histological analysis

As shown in Figure 7A and B, there were very few cells inside the scaffolds of the PCL and DTet213@PCL groups, with almost no new bone formation, and only a small amount of new bone was generated along the edges of the scaffolds. In contrast, the scaffolds of the PCL#MgP and DTet213@PCL#MgP groups contained many cells, and significant new bone formation was observed along the surfaces of the scaffolds. As shown in Figure 7C, the expression level of OPN was relatively low in the PCL and DTet213@PCL groups, whereas it was significantly upregulated in the PCL#MgP and DTet213@PCL#MgP groups. As shown in Figure 7D, the Sirius red staining results indicate that the PCL and DTet213@PCL groups were primarily composed of green type III collagen (COL-III), with the collagen fibres exhibiting a disorganized arrangement. In the

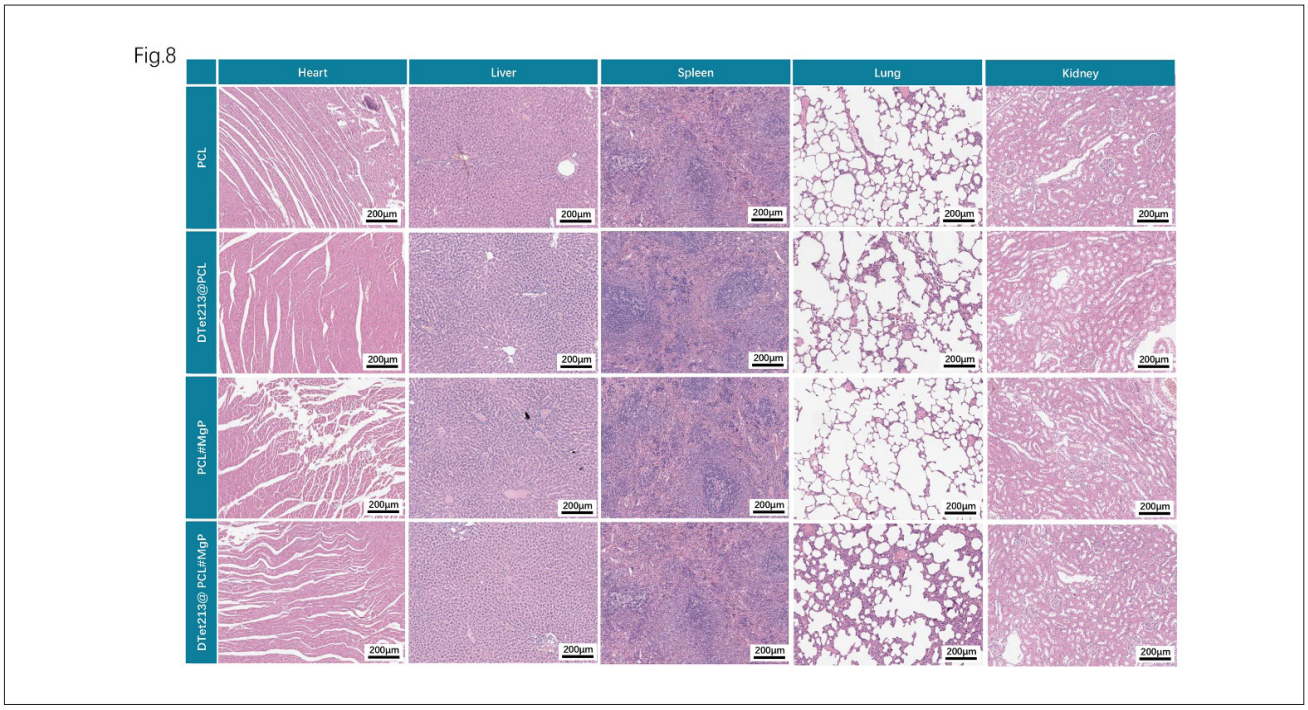

Figure 8. HE staining of the heart, liver, spleen, lung, and kidney. Scale bar: 200 μm. Abbreviation: HE, hematoxylin and eosin.

PCL#MgP and DTet213@PCL#MgP groups, the amount of yellow and red type I collagen (COL-I) significantly increased, and the collagen fibers exhibited a more orderly arrangement. In the DTet213@PCL#MgP group, the ratio of COL-I/COL-III was significantly greater than that in the PCL and DTet213@PCL groups (Figure 7E). As shown in Figure 8, HE staining was performed to observe the heart, liver, spleen, lung, and kidney of rats implanted with scaffolds from different groups. HE staining revealed no significant pathological changes or abnormalities in the heart, liver, spleen, lung, or kidney across all groups. These findings confirm the safety of the bone repair scaffold for *in vivo* implantation.

The scaffolds in the PCL and DTet213@PCL groups demonstrated inferior bone regeneration capacity because of the absence of bioactive osteogenic molecules. The scaffolds in the PCL#MgP and DTet213@PCL#MgP groups, which contained MgP that releases Mg^{2+} and PO_4^{3-} ions to promote the osteogenic differentiation of cells, demonstrated enhanced new bone formation capability. The low water solubility of MgP enables the gradual release of Mg^{2+} and PO_4^{3-} ions during degradation of the PCL scaffold, thereby promoting sustained osteogenic differentiation. The incorporation of MgP in bone repair composites, as a substitute for metallic Mg, prevents hydrogen evolution and the formation of an alkaline microenvironment associated with Mg. The DTet213@PCL#MgP scaffold, which was surface-loaded with antimicrobial peptides, shortened the early inflammatory phase of bone repair by inhibiting bacterial infection and modulating immune responses, thereby accelerating the overall regeneration process and achieving the best osteogenic outcomes.

Previous studies have shown that Mg^{2+} promotes osteogenesis by activating the canonical Wnt signaling pathway. Research indicates that treating human bone marrow stromal cells (hBMSCs) with Mg^{2+} significantly increases the expression of active β-catenin and upregulates its downstream target genes, *LEF1* and *Dkkl*, thereby inducing the differentiation of hBMSCs into osteoblasts. This mechanism reveals the osteogenic role of Mg in the bone marrow space and provides a molecular basis for its application in biodegradable implants.[28] PO_4^{3-} is a primary component in the synthesis of hydroxyapatite (HA), and its elevated local concentration can induce the synthesis of HA. Khotib et al.[29] discovered that HA can mediate the Wnt signaling pathway by regulating the expression of *Wnt10b*, *β-catenin*, *Runx2*, and Osterix (*Osx*) genes, thereby promoting the process of osteogenic differentiation. Therefore, as the scaffold degrades, the continuous release of Mg^{2+} and PO^{3-} can regulate the Wnt signaling pathway, promoting osteogenic differentiation of cells and accelerating bone regeneration.

4. Conclusion

In this study, a composite material composed of PCL and MgP was fabricated into a bone repair scaffold via FDM 3D printing, followed by surface functionalization with the Tet213 AMP with a DOPA tail. Antibacterial assays against *E. coli* and *S. aureus* revealed that both the DTet213@PCL and DTet213@PCL#MgP scaffolds exhibited significant antibacterial efficacy, which was attributed to the surface-modified Tet213 peptide with a DOPA tail. The DTet213@PCL#MgP scaffold demonstrated optimal cell adhesion and proliferation capabilities. The micro-CT results of rat tibial defect repair revealed that the DTet213@PCL#MgP scaffold presented the highest values of BV/TV, Tb.Th, and Tb.N. Histochemical staining revealed that the DTet213@PCL#MgP scaffold group presented the greatest amount of new bone formation, the highest expression of OPN, and COL-I as the primary component of the newly formed bone, with collagen fibers arranged in an orderly manner. In conclusion, the DTet213@PCL#MgP scaffold has significant application value and promising prospects in the reparation of infected bone defects.

Acknowledgments

None.

Funding

None.

Conflict of interest

The authors declare they have no competing interests.

Author contributions

Conceptualization: Ling Zheng, Ying Zhao
Formal analysis: Ling Zheng, Miao Li, Chen Liang
Project administration: Ling Zheng, Wei Zu
Visualization: Miao Li, Chen Liang, Wei Zu
Writing–original draft: Ling Zheng
Writing–review & editing: Ling Zheng, Ying Zhao

Ethics approval and consent to participate

The animal experiment in this study was approved by the Animal Research Committee of Xuanwu Hospital, Capital Medical University (License number: XW-20230520-1).

Consent for publication

Not applicable.

Availability of data

The data that support the findings of this study are available from the corresponding author upon reasonable request.

References

1. Toosi S, Javid-Naderi MJ, Tamayol A, et al. Additively manufactured porous scaffolds by design for treatment of bone defects. *Front Bioeng Biotechnol.* 2024;11:1252636. doi: 10.3389/fbioe.2023.1252636
2. Arrington ED, Smith WJ, Chambers HG, et al. Complications of iliac crest bone graft harvesting. *Clin Orthop Relat Res.* 1996;(329): 300-309. doi: 10.1097/00003086-199608000-00037
3. Yuan X, Zhu W, Yang ZY, et al. Recent advances in 3D printing of smart scaffolds for bone tissue engineering and regeneration. *Adv Mater.* 2024;36(34):e2403641. doi: 10.1002/adma.202403641
4. Cao ZM, Qin ZD, Duns GJ, et al. Repair of infected bone defects with hydrogel materials. *Polymers (Basel).* 2024;16(2):281. doi: 10.3390/polym16020281
5. Costerton JW, Stewart PS, Greenberg EP. Bacterial biofilms: a common cause of persistent infections. *Science.*1999;284(5418):1318-1322. doi: 10.1126/science.284.5418.1318
6. Yang C, Zhou L, Geng X, et al. New dual-function *in situ* bone repair scaffolds promote osteogenesis and reduce infection. *J Biol Eng.* 2022;16(1):23. doi: 10.1186/s13036-022-00302-y
7. Wright GD. The Janus effect: the biochemical logic of antibiotic resistance. *Biochemistry.* 2025;64(2):301-311. doi: 10.1021/acs.biochem.4c00585
8. Balasegaram M, Outterson K, Røttingen J-A. The time to address the antibiotic pipeline and access crisis is now. *Lancet*. 2024;404(10461):1385-1387. doi: 10.1016/S0140-6736(24)01940-8
9. Bahar AA, Ren D. Antimicrobial peptides. *Pharmaceuticals (Basel, Switzerland).* 2013;6(12):1543-1575. doi: 10.3390/ph6121543
10. Yeaman MR, Yount NY. Mechanisms of antimicrobial peptide action and resistance. *Pharmacol Rev.* 2003;55(1): 27-55. doi: 10.1124/pr.55.1.2
11. Ibrahim DM, Sani ES, Soliman AM, et al. Bioactive and elastic nanocomposites with antimicrobial properties for bone tissue regeneration. *ACS Applied Bio Materi.* 2020;3(5):3313-3325. doi: 10.1021/acsabm.0c00250

12. Lei B, Gao X, Zhang R, et al. *In situ* magnesium phosphate/polycaprolactone 3D-printed scaffold induce bone regeneration in rabbit maxillofacial bone defect model. *Mater Design*. 2022;215:110477.
doi: 10.1016/j.matdes.2022.110477

13. Zhan J, Xu H, Zhong Y, et al. Surface modification of patterned electrospun nanofibrous films *via* the adhesion of DOPA-bFGF and DOPA-ponericin G1 for skin wound healing. *Mater Design*. 2020;188:108432.
doi: 10.1016/j.matdes.2019.108432

14. Blair JMA, Webber MA, Baylay AJ, et al. Molecular mechanisms of antibiotic resistance. *Nat Rev Microbiol*. 2015;13(1):42-51.
doi: 10.1038/nrmicro3380

15. Chang DH, Lee M-R, Wang N, et al. Establishing quantifiable guidelines for antimicrobial α/β-peptide design: a partial least-squares approach to improve antimicrobial activity and reduce mammalian cell toxicity. *Acs Infect Dis*. 2023;9(12):2632-2651.
doi: 10.1021/acsinfecdis.3c00468

16. Zhang H, Jin L, Wang Q. Activities of antimicrobial peptides and the reconstruction of the natural antimicrobial peptides. *Chem Life*. 2011;31(2):227-232.
doi: 10.13488/j.smhx.2011.02.020

17. Yang C, Yu Z, Qin D, et al. Research progress in structures, mechanisms, and modification of antimicrobial peptides. *Acta Microbiol Sinica*. 2024;64(7):2242-2259.
doi: 10.13343/j.cnki.wsxb.20230812

18. Wu D, Wang L. Research progress in molecular design and optimization strategies of fish-derived antimicrobial peptides and their applications. *Chin J Anim Nutr*. 2023;35(12):7541-7551.
doi: 10.12418/CJAN2023.684

19. Ardhaoui M, Naciri M, Mullen T, et al. Evaluation of cell behaviour on atmospheric plasma deposited siloxane and fluorosiloxane coatings. *J Adhesion Sci Technol*. 2010;24(5):889-903.
doi: 10.1163/016942409x12598231567943

20. Dziadek M, Menaszek E, Zagrajczuk B, et al. New generation poly(ε-caprolactone)/gel-derived bioactive glass composites for bone tissue engineering: part I. Material properties. *Mater Sci Eng C Mater Biol Appl*. 2015;56:9-21.
doi: 10.1016/j.msec.2015.06.020

21. Zhang Y, Xu T, Li T, et al. A three-phase strategy of bionic drug reservoir scaffold by 3D printing and layer-by-layer modification for chronic relapse management in traumatic osteomyelitis. *Mater Today Bio*. 2024;29:101356.
doi: 10.1016/j.mtbio.2024.101356

22. Zhang S, Xiao Z, Luo J, et al. Dose-dependent effects of *Runx2* on bone development. *J Bone Mineral Res*. 2009;24(11):1889-1904.
doi: 10.1359/jbmr.090502

23. Bai R, Miao MZ, Li H, et al. Increased Wnt/β-catenin signaling contributes to autophagy inhibition resulting from a dietary magnesium deficiency in injury-induced osteoarthritis. *Arthritis Res Ther*. 2022;24(1):165.
doi: 10.1186/s13075-022-02848-0

24. Xu C, Guan SQ, Hou WY, et al. Magnesium-organic framework modified biodegradable electrospun scaffolds for promoting osteogenic differentiation and bone regeneration. *Eur Polym J*. 2022;181:111692.
doi: 10.1016/j.eurpolymj.2022.111692

25. Liu L, Luo P, Wen PF, et al. The role of magnesium in the pathogenesis of osteoporosis. *Front Endocrinol (Lausanne)*. 2024;15:1406248.
doi: 10.3389/fendo.2024.1406248

26. Li L, Lu H, Zhao Y, et al. Functionalized cell-free scaffolds for bone defect repair inspired by self healing of bone fractures: a review and new perspectives. *Mater Sci Eng C Mater Biol Appl*. 2019;98:1241-1251.
doi: 10.1016/j.msec.2019.01.075

27. Golafshan N, Vorndran E, Zaharievski S, et al. Tough magnesium phosphate-based 3D-printed implants induce bone regeneration in an equine defect model. *Biomaterials*. 2020;261:120302.
doi: 10.1016/j.biomaterials.2020.120302

28. Hung C-C, Chaya A, Liu K, et al. The role of magnesium ions in bone regeneration involves the canonical Wnt signaling pathway. *Acta Biomater*. 2019;98:246-255.
doi: 10.1016/j.actbio.2019.06.001

29. Khotib J, Gani MA, Budiatin AS, et al. Signaling pathway and transcriptional regulation in osteoblasts during bone healing: direct involvement of hydroxyapatite as a biomaterial. *Pharmaceuticals*. 2021;14(7):615.
doi: 10.3390/ph14070615